Kinematic variability and number of trials for studying sitting stability with spinal cord injury

Seyed Mohammadreza Shokouhyan, Mathias Blandeau, Romain Guichard, Dany H Gagnon, Thierry-Marie Guerra, Philippe Pudlo, Franck Barbier

Kinematic variability and number of trials for studying sitting stability with spinal cord injury

S. M. Shokouhyan[a], M. Blandeau[a], R. Guichard[a], D. H. Gagnon[b], T. M. Guerra[a], P. Pudlo[a] and F. Barbier[a]

[a]University Polytechnic Hauts-de-France, CNRS, UMR 8201, LAMIH, Valenciennes, France; [b]Pathokinesiology Laboratory, Center for Interdisciplinary Research in Rehabilitation of Greater Montréal, Montréal, QC, Canada

1. Introduction

In Spinal Cord Injury (SCI), maintaining the body stability is challenging due to lack of muscular activity in their lumbar level compared with healthy individuals, which makes them vulnerable during daily activities. Sitting stability is crucial in functional activities, such as wheelchair-related skills, propulsion and transfers in daily life (Potten et al. 1999). It is associated with both level and completeness of the SCI which determines the intensity of sensory, motor impairments and also sitting balance strategy (Gagnon et al. 2008; Milosevic et al. 2015).

There are several methods for assessing sitting stability in persons living with SCI. Multiple studies (Potten et al. 1999) used voluntary motor activities, albeit other studies (Blandeau et al. 2020) used resisting unexpected perturbation for understanding the underlying mechanism of sitting stability in SCI people. In both cases, these studies are based on the repetition of experimental acquisitions. Finding the Minimum Number of Trials (MNT) not only does shorten the time of testing, but also reduces the risk for any potential injury during acquisitions.

Previous studies used different strategies for finding the MNT in clinical tests. Severing et al (Severin et al. 2021) calculated the MNT in 10 recreational golfers during swing. In their study they used various reliability methods like sequential analysis method (SAM) and intraclass correlations (ICC) on the kinetic kinematic data. Same as the aforementioned study, the purpose of this study is to determine the MNT to achieve stability of variables studied in clinical tests of SCI by SAM and ICC methods.

2. Methods

2.1. Participants

Five subjects (three men and two women, 39.8 ± 11.9 years old) living with an SCI (ASIA A, level of injury at T4, T5 and T6) participated in this study. Ethical approval has been obtained from the Research Ethics Committee of the Centre for Interdisciplinary Research in Rehabilitation of Greater Montreal (CRIR-1083-0515R).

2.2. Experimental procedure

Participants maintained a sitting position without back support with hip and knees flexed to 90°, feet resting on the floor (Figure 1). Light horizontal destabilizing forces were randomly applied in 12 acquisitions at the level of the 3rd thoracic vertebra between the scapulae via a foam-coated wooden pole to which a pressure sensor was added on the tip to define the contact instant.

Subjects' tasks were to maintain their challenged stability by moving their upper limbs back and forth. To record the kinematics, 39 skin-fixed infrared light-emitting diodes were attached on the participant's body. Kinematics data were recorded at 60 Hz using a 4-camera Optotrak system (NDI, Waterloo, Canada). The trial start time was vocally announced to participants, at which time they rose their arms and maintained their stability before the perturbation. Their stability was visually assessed by the examiner, and the time instant was recorded by a synchronized hand switch. Then, the perturbation was exerted at a random time, and participants should have regained their stability. Their status was again visually assessed, and the time instant recorded when they achieved their stability. All four-time instants sampled at 600 Hz and then were down sampled to 60 Hz to match with the kinematics data. To reduce measurement noise, all kinematics signals were filtered with a low-pass four-order Butterworth filter with a cutoff frequency of 6 Hz (Gagnon et al. 2008).

2.3. Data analysis

The distance between marker attached on T3 and the middle point of right and left forearm medial condyles was calculated 3 seconds after the perturbation. The distance signals were then numerically differentiated to yield the velocity signals. In order to perform the sequential analysis, several parameters such as standard deviation (SD), range and mean value of both distance (in mm) and velocity (in mm/s) signals were computed as well as the exact time interval between the perturbation instant and the time when stability was regained (determined visually by the same operator for all acquisitions). Reliability analysis was performed on the kinematic variability parameters using the ICC model (MNT defined as trial when ICC is maximal, (Gore et al. 2016)). The sequential

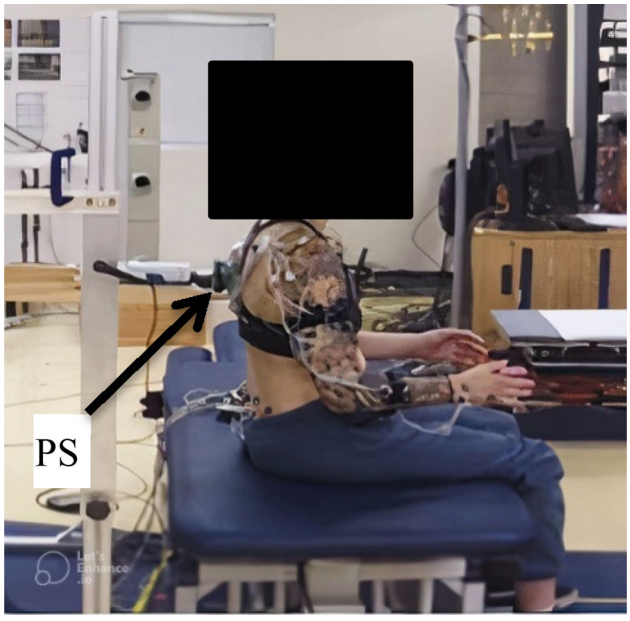

Figure 1. Experimental Setup (PS: Pressure Sensor, placed at the tip of the destabilizing device)

analysis was used by two methods based on the standard deviation with 2 thresholds of a) 20% of SD b) 30% of SD (MNT defined as trial when parameter crosses threshold (Gore et al. 2016)) for 12 acquisitions in each participant. All data analysis was performed by Matlab@R2021b software. The MNT will be determined by the sequential parameter which produces the most conservative and stable result.

3. Results and discussion

MNT in each method were shown in Table 1. The ICC method indicated between 2 to 5 required trials which are fewer compared with other two methods. The sequential analysis with SD_{20} and SD_{30} suggest at least 9 to 10 required trials. In addition, in one study (Severin et al. 2021), the number of required results in the standard deviation strategy was larger compared with ICC method. The ICC method showed the smaller MNT between other methods, which demonstrates that the kinematics variability will be stable just after 5 trials. Although, SD_{20} and SD_{30} showed the most conservative results in MNT, on the other hand, it should be noted that method such as SAM has the least limitation compared with other methods (Gore et al. 2016). The analysis showed that the MNT varied between different kinematic variables. Furthermore, the values of MNT computed on two parameters of mean velocity and stability time were smaller in both two methods of SD_{20} and SD_{30} compared with other parameters. Except SD and range of velocity and mean distance, other parameters demonstrated conservative results among two strategies. In addition, it should be mentioned that the learning parameter from the experimenter affected the value of stability time. Although, the MNT should be based on the study task, but this study suggests that 9 to 10 trials would be sufficient for the biomechanical analysis in SCI patients.

Table 1. MNT (mean (SD)) for each kinematic parameter.

Variable \ Method	SD_{20}	SD_{30}	ICC
Mean distance	**8 (1.92)**	**7 (1.50)**	**5**
Mean velocity	**6 (1.64)**	**6 (1.47)**	**3**
Distance Range	**7 (2.28)**	**7 (1.72)**	**4**
Velocity Range	**7 (2.30)**	**6 (1.47)**	**4**
SD of distance	**7 (1.79)**	**7 (1.41)**	**5**
SD of velocity	**8 (0.84)**	**6 (2.14)**	**4**
Stability time	**6 (1.95)**	**6 (1.6)**	**2**

4. Conclusions

In this study the MNT was investigated based on the sequential analysis of kinematic data from SCI patients. Twelve acquisitions were performed in presence of external perturbation during sitting on SCI. kinematic parameters were calculated in 3 seconds after the perturbation time instant. The sequential analysis result indicated that SD_{20} and SD_{30} methods produced the most conservative MNT, and this study suggests 9 to 10 trials for biomechanical analysis of SCI individuals.

Funding

This work is supported by the French Ministry of Higher Education, Research and Innovation, the National Center for Scientific Research (CNRS), Zodiac Seat France and Direction Générale de l'Aviation Civile (project no 2014 93 0818).

References

Blandeau M, Guerra T-M, Pudlo P. 2020. Application of a TS unknown input observer for studying sitting control for people living with spinal cord injury. In: Control applications for biomedical engineering systems. London: Elsevier; p. 169–195.

Gagnon D, Nadeau S, Desjardins P, Noreau L. 2008. Biomechanical assessment of sitting pivot transfer tasks using a newly developed instrumented transfer system among long-term wheelchair users. J Biomech. 41(5): 1104–1110.

Gore SJ, Marshall BM, Franklyn-Miller AD, Falvey EC, Moran KA. 2016. The number of trials required to obtain a representative movement pattern during a hurdle hop exercise. J Appl Biomech. 32(3):295–300.

Milosevic M, Masani K, Kuipers MJ, Rahouni H, Verrier MC, McConville KMV, Popovic MR. 2015. Trunk control impairment is responsible for postural instability during quiet sitting in individuals with cervical spinal cord injury. Clin Biomech. 30(5):507–512.

Potten YJM, Seelen HAM, Drukker J, Reulen JPH, Drost MR. 1999. Postural muscle responses in the spinal cord injured persons during forward reaching. Ergonomics. 42(9):1200–1215.

Severin AC, Barnes SG, Tackett SA, Barnes CL, Mannen EM. 2021. The required number of trials for biomechanical analysis of a golf swing. Sports Biomech. 20(2): 238–246.

KEYWORDS Spinal cord injury; sequential analysis method; intra class correlation

Mathias.Blandeau@uphf.fr

IMU based simulation of a Musculo-skeletal model of the lower limb

F. Soussi[a], A. Tayari[a], T. Rezgui[b], A. Houidi[a] and S. Bennour[a]

[a]The Mechanical Laboratory of Sousse 'LMS', University of Sousse, Sousse, Tunisia; [b]Applied Mechanics, and Systems Research Laboratory (LASMAP), Polytechnic School of Tunisia, University of Carthage, Carthage, Tunisia

1. Introduction

Nowadays, human motion analysis is very important for several fields particularly in the assessment of a person's gait condition, medical diagnosis and rehabilitation, athletic performance evaluation and monitoring (Perry and Burnfield 2010). In the beginning, orthopaedists and podiatrists used to perform qualitative diagnoses relying only on observations. However, thanks to the technological enhancements, several technologies (optical cameras, Inertial sensors, Kinect, …) were developed in order to assist specialists giving them the ability to perform a more accurate diagnose through 3D joint kinematics (Al Borno et al. 2022).

The aim of this paper is to present a customized low cost, wireless and compact system based on inertial measurement units that realizes the acquisition of joints angles of the lower limb that gives us the possibility to perform the characterization of human motion in real environment (i.e; in situ or ecological), and then to evaluate of our system's performances.

2. Methods

The IMU's (inertial measurement units), are micro-electromechanical inertial sensors composed of three axis gyroscopes, accelerometer and in our case magnetometer. Took each one on its own, the outputs cannot measure the orientation. Nevertheless, using a fusing filter, the sensor orientation in a global coordinate system can be secured. In other hand, skeletal system is represented as linked-rigid bodies representing major bones or groups of bones. In our study, a single leg is modeled as four segments: the pelvis, the femur, tibia-fibula segment, and foot. The corresponding joints, namely the hip, knee, and ankle have 3 rotations as degrees of freedom (Dof) (Cappozzo et al. 2005). Now, at least one IMU on each body segment is needed to obtain the variation of joint kinematics.

To carry out the study, we chose the open-source software OpenSim that allows the creation of musculoskeletal models modify them and animate them to simulate movements, giving us the ability to plot the joint segments variation using the variation of the fused data extracted from the measuring units.

2.1. Experiment protocol

Different phenomena have to be considered while doing the experimentation, one of them is the soft tissue artefact (STA) that can cause large errors. In order to minimize this issue, the acquisition systems were fixed on the segments at the boniest areas.

Two calibration phases are necessary. The first one is needed to eliminate the offsets of the measuring units. This phase is performed on a flat surface by executing different angles before fixing the sensor on the subject. The second one is performed to provide the orientation of the segment coordinate system according to the IMU coordinate system based on a sensor to segment calibration (Pacheret al. 2020).

2.2. Data acquisition

An acquisition system based on inertial units has been developed; each system includes a 9 Dof inertial sensor (MPU9250) and a microprocessor (ESP8266) that will treat the data and a Wi-Fi module to transfer the row data from the microprocessor to the PC where the data will be processed (Figure 1).

In this study, a female (25 years, 1.65m height and 64 Kg) had participated to experimentation. Four systems are used on the right lower limb. The pelvis sensor was placed on the sacrum. The IMU describes a coordinate system defined as x-axis pointing cranially and z-axis pointing posteriorly. The thigh sensor was placed on the iliotibial tract approximately 6 cm above the patella. The shank sensor was positioned on the middle of the fibula. The sensors on thigh and shank were positioned with x-axis pointing cranially and z-axis pointing laterally. The foot sensor was positioned with x-axis pointing cranially and z-axis pointing laterally on the dorsal region of the foot.

2.3. Data fusion

To get an optimal result in term of position of the body segments, it is necessary to go further than using the raw data of the sensor since the gyroscope data deviates with time and the magnetometer can be easily disturbed. Therefore, to make a compromise and take the best of all unit of measurement, we will use the internal fusion algorithm.An internal fusion algorithm takes as input the data of the accelerometer, gyroscope and magnetometer to combine them and finally give the orientation of the body segments as output.In general, the angular position is represented

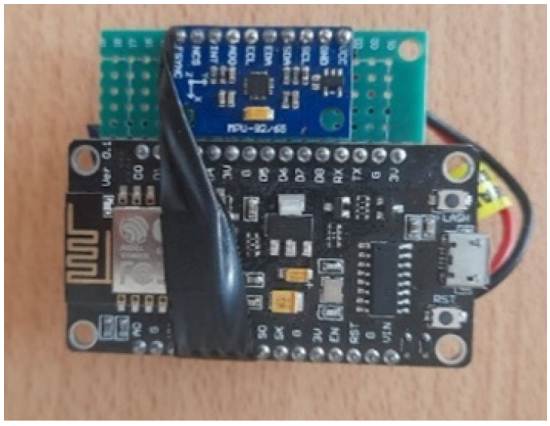

Figure 1. ESP8266 board with MPU9250 and batterie.

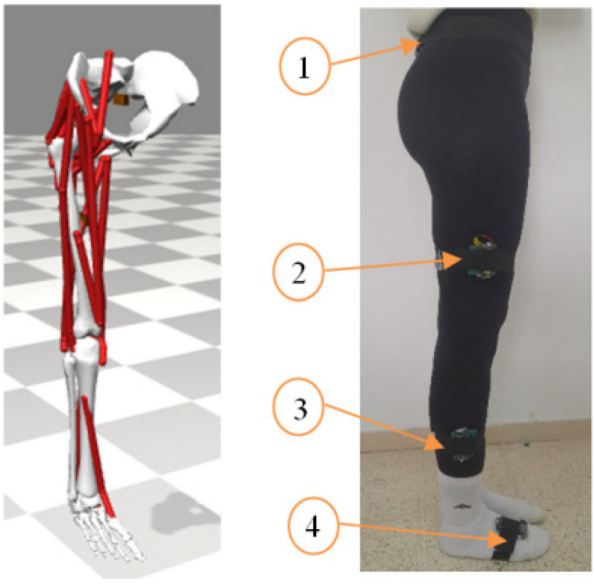

Figure 2. Geometric model on OpenSim and IMU placement on the subject.

by a quaternion, because it is acompact and singularity-free, and it can be quickly converted back to a rotation matrix or Euler angles. The commonly used filters are the Kalman filters with their different formulations. Some comparative studies have been carried out to determine the most effective filter, even during our work; we used different filters before finally adopting the more accurate one, which is the double stage filter (Sabatelli et al. 2013).

2.4. Skeletal modelling

The model used to carry on this study was the Leg6Dof9Musc model from Opensim library, modifications were added to this model to make it more adapted to our work, the model was upgraded from 5 Dof to 9 Dof, three rotations at each joint (Figure 2).

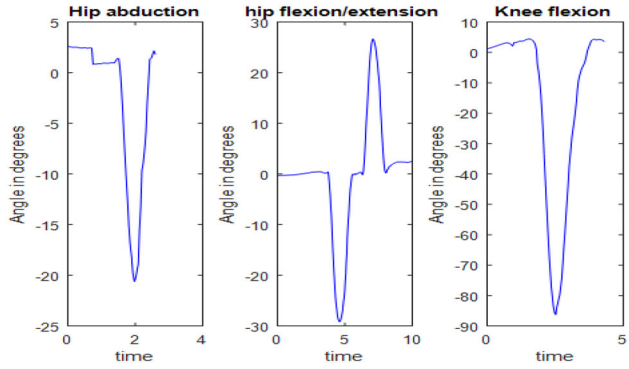

Figure 3. The computed kinematics via OpenSim.

In order to realize the scaling of the model, we need to calculate the quaternions at static pose. The computed data needs to be adapted to the format of the software (.sto file).

Kinematic joints were determined through OpensSense package for kinematic analysis from IMU.

3. Results and discussion

The subject is asked to perform simple tasks. A flexion-extension of the hip, an abduction-adduction of the hip and a flexion-extension of the knee. The results obtained are represented in Figure 3. The obtained angular patterns and range of motion are within the forms and range of a normal healthy individual. The estimated angles are equal to the expected values and consistent with the joint's rotations.

4. Conclusions

In this work, we represented an embedded device based on commercialized and low cost IMUs that enable us to compute the joint angle of the lower limb using the variation of quaternions collected from the measurement units and processed through the OpenSim software. This device is a preliminary work which we intend to improve in order to create a low cost system that permit the realization of motion analysis.

Disclosure statement

No potential conflict of interest was reported by the authors.

References

Al Borno M, O'Day J, Ibarra V, Dunne J, Seth A, Habib A, Ong C, Hicks J, Uhlrich S, Delp S. 2022. OpenSense: An open-source toolbox for inertial-measurement-unit-based measurement of lower extremity kinematics over long durations. J Neuro Eng Rehabil. 19(1):22.

Cappozzo A, Dellacroce U, Leardini A, Chiari L. 2005. Human movement analysis using stereophotogrammetry

Part 1: theoretical background. Gait Posture. 21(2): 186–196.

Pacher L, Chatellier C, Vauzelle R, Fradet L. 2020. Sensor-to-segment calibration methodologies for lower-body kinematic analysis with inertial sensors: a systematic review. Sensors. 20(11):3322.

Perry J., Burnfield JM. Gait analysis: normal and pathological function. J Sports Sci Med. 2010; 9(2):353.

Sabatelli S, Galgani M, Fanucci L, Rocchi A. 2013. A double-stage Kalman filter for orientation tracking with an integrated processor in 9-D IMU. IEEE Trans Instrum Meas. 62(3):590–598.

KEYWORDS Motion analysis; IMU sensors; OpenSim; OpenSense; kinematics

fatma.soussi@eniso.u-sousse.tn

Wearable sensors-based three-dimensional knee kinematics during gait for healthy subjects and osteoarthritis patients

A. Tayari[a], T. Rezgui[b], F. Soussi[a], K. Grariri[a], S. Baklouti[a], M. Saafi[d], K. Ben Mansour[c], F. Marin[c] and S. Bennour[a]

[a]Mechanical Laboratory of Sousse 'LMS', University of Sousse, Sousse, Tunisia; [b]Applied Mechanics, and Systems Research Laboratory (LASMAP), Polytechnic School of Tunisia, University of Carthage, Carthage, Tunisia; [c]eSorbonne Universities, University of Technology of Compiegne, BMBI UMR CNRS 7338, Sorbonne, France; [d]Laboratory of Technology and Medical Imaging 'LTIM', University of Monastir, Monastir, Tunisia

1. Introduction

Knee osteoarthritis (OA) is a common musculoskeletal condition affecting millions of people worldwide. It is clinically associated with pain and stiffness leading to reduced joint mobility and progressive gait dysfunction (Hunt et al 2011). Measure and identify 3D knee gait kinematic differences related to the presence of OA is crucial for treatment and pursuing progression. Several technologies for motion analysis are used, including camera fusion (Tayari et al. 2021) and wearable inertial measurement units MIMU which present a revolutionary tool in gait analysis specially for outdoor applications. The new study of Hafer et al investigate the validity of MIMU compared to MOCAP and the kinematic differences for healthy young participant, older adults, and older adults with knee osteoarthritis (Hafer et al 2022). The study is one of the most profound evaluations of OA gait kinematic. However, its strong limitation is that only one single degree of freedom is considered for the knee (flexion-extension), while knee adduction abduction is highly altered by osteoarthritis severities (Kean et al 2012). The objective of this preliminary study is to investigate the possibility to estimate 3D knee kinematics using MIMUs in patients with OA and the differences between patients with OA and a control group.

2. Methods

2.1. Participants

Eight healthy participants (28.7 ± 4.2 yrs), and eight patients with knee OA (69.2 ± 4.6 yrs) were considered. The database contains data from four MIMUs (APDM Opal, USA, sampling frequency: 128 Hz) located on the sacrum, thigh, shank, and left foot in typical participants or the leg with the more important radiographic osteoarthritis severity for patient with knee osteoarthritis. Participants were asked to perform static pose and walking trials with a comfortable range of motion and velocity. At least 10 motion cycle were collected. Data collection was carried out. permanently, and sensors were synchronized to each other throughout the test. The 3D orientation of each MIMU was obtained through a Kalman filter embedded in the devices (Holmstrom 2016).

2.2. Inverse kinematics modelling

Inverse kinematic modeling allows to obtain the joint angles from the inertial data. To achieve this, we used OpenSense which is a workflow that enables to compute the motions of body segments based on MIMU data. OpenSense link and register each MIMU sensor with a body segment of an OpenSim model. In our study we used Leg6Dof9Musc OpenSim model, virtual MIMU sensors were placed on the geometric model. Calibration was performed based on the static data that preceded the walk for each trial. Static data which the participant stand in an almost neutral position. In fact, OpenSense calibration save relative sensors orientations in the global frame of the model. Ten walk cycles from each test subject was used to calculate mean knee flexion extension, abduction adduction, and internal external rotation during walk cycle. After compiling inverse kinematic the output data was segmented using MATLAB and normalised to to 0–100% of the gait cycle.

3. Results and discussion

The figure bellow (Figure 1) presents the mean angles of each subject.

For healthy participants the angles obtained correspond to the measurements in the literature (Nouma et al. 2018). We calculate interclass correlation coefficient ICC to evaluate inter-subject variability, the correlation between adduction abduction angle is the lowest. However, it remains in the standard of moderate agreement. For patients with knee osteoarthritis, maximum flexion during stance phase was remarkably lower compared to healthy participants, respectively (8.5°±3.6°, 17.5°±4.7°). Also, during swing phase of osteoarthritis patients there is a decreasing in flexion compared to healthy participants (55.4°±8.2°, 47.15°±2.6°). For adduction abduction angles OA patients have a range of motion lower than typical participants (3.8°±2°) compared to (6.7°±5.2°). Figure 2 illustrate mean knee rotations of healthy and OA individuals.

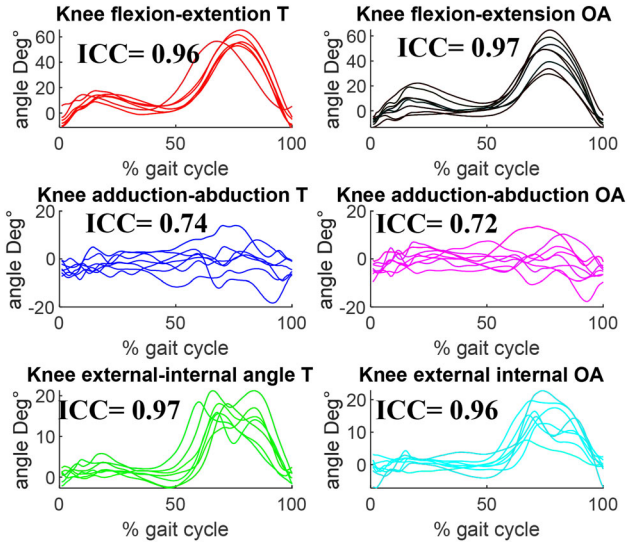

Figure 1. Mean knee angles for typical (T), knee osteoarthritis (OA) participants.

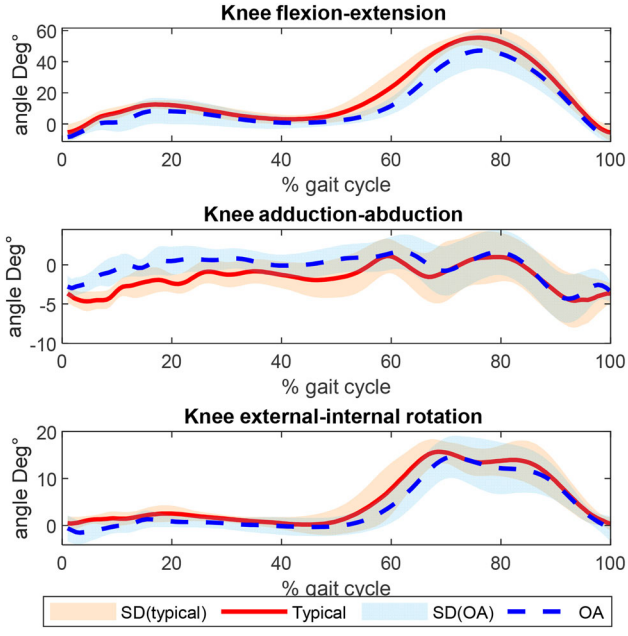

Figure 2. Mean knee kinematics curves during gait cycle with standard deviation.

As previous studies have shown, in the presence of knee OA human body adopt a protective mechanism to avoid loading the affected knee during walking reducing knee flexion angles during the stance phase of walking (Al-Zahrani and Bakheit 2009). However, knee adduction abduction disparities may indicate severity degree of OA and deserve further attention. Also, an interesting behavior of knee internal external rotation showing in Figure 1 and my reveal OA characteristics and have to be deeply investigated, it may be an initiation of diagnostics and rehabilitation protocol based on wearable sensors and movement correction as suggested in the study of Edd et al. (2020).

4. Conclusions

This work is a preliminary study to investigate the 3D knee kinematics in patients with OA using MIMUs and to compare pathological kinematics with that obtained in healthy participants. The estimation of knee abduction adduction and internal and external rotation is extremely challenging using wearable magnetic-inertial as several errors may affect the procedure. The obtained results are promising in term of the presence and progression of knee osteoarthritis indicator and may be an alternative tool of diagnostics and rehabilitation protocol based on wearable sensors and movement corrections.

References

Al Borno M, O'Day J, Ibarra V, Dunne J, Seth A, Habib A, Ong C, Hicks J, Uhlrich S, Delp S. 2022. OpenSense: an open-source toolbox for inertial-measurement-unit-based measurement of lower extremity kinematics over long durations. J Neuro Eng Rehabil. 19(1):22.

Tayari A., S. Baklouti, M. Saafi, S. Bennour. 2021. Real-time fusion of upper-limb kinematic measurements from dual-kinect CMBBE 24(sup1), pp. S89–S90

Al-Zahrani KS, Bakheit AMO. A study of the gait characteristics of patients with chronic osteoarthritis of the knee. Disabil Rehabil. 2009;24(5):275–80.

Edd SN, Vida Martins N, Bennour S, Ulrich B, Jolles BM and Favre J. 2020. Changes in lower limb biomechanics when following floor-projected foot placement visual cues for gait rehabilitation. Gait Posture. 77:293–299.

Hafer JF, Mihy JA, Hunt A, Zernicke RF, Johnson RT. 2022. IMU-derived kinematics detect gait differences with age or knee osteoarthritis but differ from marker-derived inverse kinematics.

Holmstrom L. 2016. Using orientation estimates to convert from sensor frame to Earth frame of reference https://support.apdm.com/hc/en-us/articles/214504186-Using-orientation-estimates-toconvert-from-sensor-frame-to-Earth-frame-of-refernce (accessed 11 March 2021).

Hunt MA, Schache AG, Hinman RS, and Crossley KM. 2011. Varus thrust in medial knee osteoarthritis: quantification and effects of different gait-related interventions using a single case study. Arthritis Care Res. 63, 293–297

Kean CO, Hinman RS, Bowles KA, Cicuttini F, Davies-Tuck M, and Bennell KL. 2012. Comparison of peak knee adduction moment and knee adduction moment impulse in distinguishing between severities of knee osteoarthritis. Clinical Biomech. 27(5):520–523.

Nouma BB, Mitiche A, Ouakrim Y, Mezghani N. 2018. Knee kinematic curve representation and application to knee pathology classification. JBEI. 4(1):32.

KEYWORDS Knee osteoarthritis (OA); IMU; OpenSim; OpenSense; kinematics

tayari.azza@eniso.u-sousse.tn

Using external back shape curvature to predict internal vertebrae positions in sitting postures: preliminary results

A. Tomezzoli[a], A. Agouram[a], B. Chalamet[b], J. B. Pialat[b,c], S. Duprey[a] and B. Fréchède[a]

[a]Univ Lyon, Univ Gustave Eiffel, Univ Claude Bernard Lyon 1, LBMC UMR T_ 9406, Lyon, France; [b]Service de Radiologie, Hôpital Lyon-Sud, HCL, Pierre-Bénite, France; [c]Laboratoire CREATIS, Unité CNRS UMR 5220 – INSERM U1294 – Univ Lyon 1 – INSA Lyon – Univ Jean Monnet Saint-Etienne, Villeurbanne, France

1. Introduction

Predicting vertebrae positions in different spinal postures from external data, using a single regression for each vertebra, could be interesting for clinical and ergonomics applications by limiting the exposure to radiation. With a limited set of markers, Nerot et al (2018) achieved one of the best predictions with a geometrical method, reaching an average error of 10.2 ± 5.6 mm between the predicted position of intervertebral joint centres and their actual position on radiographs for C7-T1 to L5-S1 intervertebral joints. The prediction model was specific to a free-standing posture.

The aim of our study was to build models which are valid and robust in several seated spinal postures. To achieve this goal, predictors that are correlated to spinal postures should be added to existing models. We hypothesized that external back shape curvatures are important predictors of vertebrae positions. As a first step to assess this hypothesis, univariate statistical models were built; only the best coefficients of determination (R^2) of models from C4 to Th10 vertebrae were considered and presented in these preliminary results.

2. Methods

2.1. Data collection

Twenty-one healthy participants (13 females, 23.6 ± 4.4 years, BMI 21.9 ± 1.5 kg/m^2) were recruited after ethical endorsement (CPP N°2020-A00573-36). Cutaneous markers were positioned facing C4 to T10 spinous processes, by manual palpation. Low dose radiographs (EOS® Imaging, France) were taken in 3 postures: slouched, erect and the usual sitting posture of the participants (called reference).

Superior-posterior vertebral corner (Klinich et al. 2012) and cutaneous markers coordinates were extracted using a Matlab toolbox (Gasparutto and Tomezzoli 2021). Furthermore, to quantify the magnitude of the differences between spinal postures, the C2-C7 cervical lordosis and T1-T12 thoracic kyphosis angles were measured using the 2D tool SterEOS® (EOS® imaging, Paris, France).

2.2. Building of the curvilinear frames

To represent the back shape, external markers were fitted using the cubic spline function csaps of Matlab (The MathWorks I 2021). The smoothing parameter value $p = 10^{-4}$ was chosen based on graphical criteria, to reach a compromise between smoothness and proximity to external markers at the thoracic level. At the cervical level, a more flexible spline was needed; this is consistent with the literature, as the intervertebral range of motion is higher at the cervical spine than at the thoracic spine levels (White and Panjabi 1990). Consequently, C4 to C6 markers were weighted more than T2 to T10 markers (weights $w = 32$ versus 1), C7 and T1 being weighted with intermediate values to ensure continuity.

The spline was discretized into approximately 30 000 points equally distributed along their absolute vertical coordinate. The resulting distances between two consecutive spline points never exceeded 0.02 mm. The external markers were then projected perpendicularly on the spline (P points). Tangents and normals were computed to build curvilinear Frenet frames at each P point. All normals were then orientated forward in relation to the participant (Figure 1).

2.3. Variables and statistics

The distance (d) between each P point and its vertebral upper-posterior corner counterpart was computed, along with the angle (α) between this segment and the spline normal. Furthermore, at each P point, the spline curvature (k) was calculated as a derivative of the tangential vector with respect to the curvilinear distance, with a negative sign if its direction was opposite to the normal vector direction (i.e. for lordosis).

The statistical significance of the effect of posture on C2-C7 angles, T1-T12 angles and spine curvatures was assessed using linear models (R Core Team 2018). The statistical links between external curvatures and distance d and angle α were computed at each P point, using univariate linear models. After visually checking for model residuals' normality, the model yielding the best R^2 for each vertebra was reported.

3. Results and discussion

3.1. Descriptive statistics

The C2-C7 angle was 15.3° ± 10°, 25.3° ± 10.1° and 40.7° ± 13.8° in the erect, reference and slouched

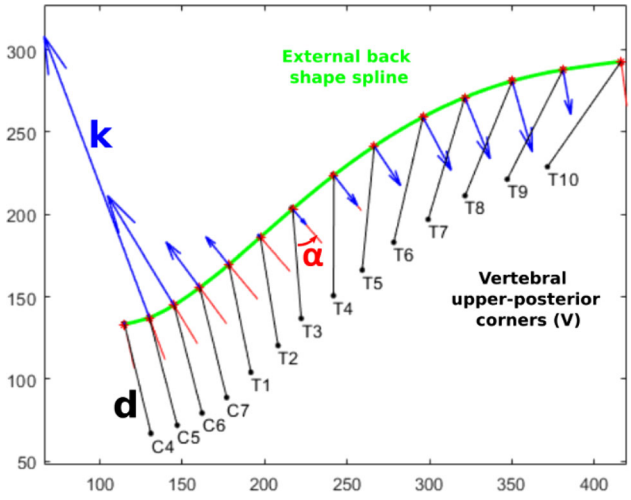

Figure 1. Back parameters. *Red points: projection of cutaneous markers on the spline (P). Red lines: normal vectors directions (N). Blue arrows: spline curvatures (k), α: angle (PV, N), d: distance [PV].*

postures, respectively; the T1-T12 angle was 28.7° ± 9.1°, 37.5° ± 11.2° and 54.3° ± 12.4° in those postures, a negative sign indicating a kyphosis. Mean curvatures (k) ranged from $-0.0181\,mm^{-1}$ at C6 to $0{,}0033\,mm^{-1}$ at T7 level. Mean angles (α) ranged from −0.1° at the C4 vertebra level to 40.7° at T10. Mean distances (d) ranged from 61.1mm at C5 to 75.4mm at T10 level.

Postures were distinctive to each other in terms of C2-C7 angles ($p < 0.001$), T1-T12 angles ($p < 0.001$) and spline curvature in C4 ($p < 0.01$), C5 ($p < 0.001$), C6 ($p < 0.01$), T1 ($p < 0.01$), T2 ($p < 0.05$), T5 ($p < 0.01$) and T6 to T10 ($p < 0.001$).

3.2. Predictive ability of spline curvatures

Maximal R^2 of models for angles (α) prediction ranged from 0.21 to 0.61 ($p < 0.001$). They were mostly associated with spline curvatures located around C7 (Table 1). Maximal R^2 for distances ranged from 0.17 to 0.31 ($p < 0.001$), associated with spline curvatures located around C7 and from T6 to T10.

4. Conclusions

To assess the relevance of using back shape curvatures as predictors of vertebrae positions in various spinal postures, statistical links between vertebrae positions, expressed in local curvilinear frames, and local back shape curvatures were computed. Coefficients of determination of a model usually increase along with the number of variables included in the model. The models built by Nerot et al (2018) included 1 to 4 variables and had R^2 ranging from 0.4 to 0.8, depending on the vertebral joint level. The order of magnitude of R^2 in our study seem therefore high enough to consider the back shape curvature as an additional potential predictor of vertebrae positions; as curvatures are related to spinal posture, this parameter could help build models which are valid in several spinal postures. This should allow improving subject specific manikins and might help monitoring the risk of vertebrae fractures in osteoporotic patients. To further this preliminary analysis, multivariate regressions that include usual predictors, e.g. related to participants' anthropometry might be built and a validation analysis conducted.

Table 1. Best predictors, among spline curvatures, for distance d and angle α.

	Best predictors for	
Vertebrae	Angle α (R^2)	Distance d (R^2)
C4	kC6 (0.53)	kC6 (0.29)
C5	kC7 (0.48)	kT6-kT7 (0.30)
C6	kC6 (0.46)	kT6 (0.31)
C7	kC7 (0.61)	kT6 (0.19)
T1	kC7 (0.33)	kT1 (0.17)
T2	kT5 (0.26)	kC7 (0.21)
T3	kT5 (0.35)	kC7 (0.22)
T4	kC7 (0.30)	kC7 (0.27)
T5	kC7 (0.24)	kT10 (0.23)
T6	kC7 (0.22)	kT10 (0.25)
T7	kT1 (0.24)	kT9 (0.24)
T8	kT1 (0.32)	kT9 (0.26)
T9	kT1 (0.33)	kT8-kT10 (0.25)
T10	kT1 (0.21)	kT8, kT10 (0.22)

Disclosure statement

No potential conflict of interest was reported by the authors.

References

Gasparutto X. Tomezzoli A. 2021. EOS_data_extraction at UpperLimb_Spine. GitHub [Internet]. [accessed 2021 Nov 4]. https://github.com/A-Tomezzoli/EOS_data_extraction

Klinich KD, Ebert SM, Reed MP. 2012. Quantifying cervical-spine curvature using Bézier splines. J Biomech Eng. 134(11):114503.

Nerot A, Skalli W, Wang X. 2018. Estimation of spinal joint centers from external back profile and anatomical landmarks. J Biomech. 70:96–101.

R Core Team. 2018. R: A language and environment for statistical computing. [Internet]. Vienna, Austria: R Foundation for Statistical Computing. http://www.R-project.org.

The MathWorks I. 2021. Curve Fitting Toolbox [Internet]. Natick. Massachusetts. United States. https://www.mathworks.com/products/curvefitting.html

WhiteAA. Panjabi MM. 1990. Clinical Biomechanics of the Spine. Lippincott. Philadelphia.

KEYWORDS Spine; sitting position; posture; models

bertrand.frechede@univ-lyon1.fr

Vertebral bone density investigation

F. Tomi, L. Leblond, Y. Godio-Raboutet, R. La Greca and M. Evin

Laboratoire de Biomécanique Appliquée, Aix-Marseille Univ, Univ Gustave Eiffel, IFSTTAR, LBA, Marseille, France

1. Introduction

Experimentation on human spine investigation matter associated with surgical practices, such as simulation of perforation or pull out, is performed upon cadaver, animal, or synthetic vertebrae. However, availability, ethical concerns, preservation method, associated cost as well as suitability of such material should be considered when choosing surrogate for human spine.

Human cadaver samples have some limitations: age of the subject, associated potential osteoporotic state as well as preservation procedure can impact the mechanical structure of the bones (Stefan et al. 2010). In synthetic material, one must notice the limitation of available vertebra (both quantity and variety) in manufacturer catalogue as well as availability of the validation data in term of material properties and associated cost.

Material properties are closely correlated to bone density (Morgan et al. 2003; Morgan et al. 2018), meaning that density analysis can be used as a tool to design new materials close to a specific subject type.

The aim of this study is to investigate the vertebral density measurement in human, swine, and synthetic vertebrae to identify the most suitable material for mimicking in-vivo spine vertebra, for surgical training and studies purposes.

2. Methods

CT (computed tomography) scans were used to assess the density of both cortical and trabecular bone in three different samples:

- 14 swine vertebrae (two swines – approximately 4 months old and 60 Kg, landrace swine) – (government agreement number C-013-15-022; Ethical committee CEEA 14)
- 15 human vertebrae (from 3 cadavers – Age 77 to 94 – all male) – human tissue testing controlled by the Medicine Faculty in Marseille according with the 76-435 decree and extraction protocol approved by the local ethics committee.
- 3 synthetic vertebrae (Sawbones, Washington, USA): rigid polyurethane foams with reported density (10% tolerance) as: PCF 5: 80mg/cc; PCF 10: 160mg/cc; PCF 20: 320mg/cc (compression modulus of 16MPa, 38MPa, 210MPa, respectively).

The Hounsfield Unit (HU), associated to greyscale of CT modality, is defined and calibrated per-machine with air and water linear attenuation coefficients (Aamodt et al. 1999; Lim Fat et al. 2012; Patrick et al. 2017). An electron density phantom (Model 062M, CIRS Inc. Virginia, USA) with three calibrated plugs (200, 800 and 1250 mg/cc), was used to calibrate densities in (mg/cc) as linear regression between the three computed HU reference values of selected volume of the plugs.

Manual thresholding (ParaView software (AHRENS et al. 2005)) was applied to 3D CT scan volume. Bandpass filters for cortical and trabecular bones, and phantom references values were selected. Histograms of the HU distributions for cortical and trabecular bones were identified and HU median values were computed and converted to mg/cc for both bones.

Vertebrae were grouped par type: high thoracic, low thoracic and lumbar vertebrae. Plots and computations were performed using matplotlib library in python and Scipy for statistical analysis. Comparison between groups were performed using Kruskal-Wallis

3. Results and discussion

A total of 29 vertebrae have been analyzed, and categorized as such:

- High thoracic: T2, T3, T4
- Low thoracic: T9, T11, T12
- Lumbar: L1, L5

Swine cortical vertebral bone densities were found lower through the whole spine when comparing spinal location by location with human vertebrae densities except for the lumbar vertebrae (from 15 to 50%, high thoracic: $p = 0.012$, low thoracic: $p = 0.053$) (Figure 1). Trabecular vertebral densities along the spine in swine model seems to increase toward lumbar location. On the contrary, in human model, lumbar vertebrae showed lower densities than high thoracic ones (while not showing any significance). Comparison with literature could be found in (Morgan et al. 2018). Differences between swine and human vertebrae could be highlighted especially on the spinous process and orientation of articular process.

Synthetic material density has been considered as not representative as negative in term of handful unit.

Table 1. Human and swine median densities.

Vertebra	Human cortical (mg/cc)	Swine cortical (mg/cc)	Human trabecular (mg/cc)	Swine trabecular (mg/cc)
High thoracic	613.1 ± 110.44	389.95 ± 79.63	248.77 ± 110.96	129.58 ± 62.9
Low thoracic	552.85 ± 132.25	397.95 ± 105.72	125.92 ± 153.57	153.42 ± 96.69
Lumbar	552.93 ± 146.38	466.12 ± 118.48	131.66 ± 88.34	195.86 ± 94.02

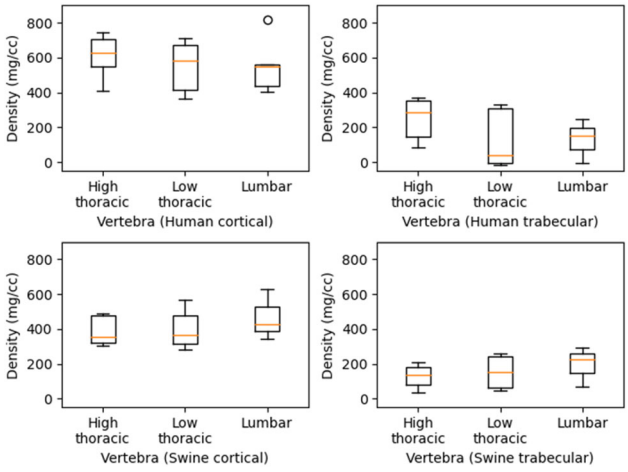

Figure 1. Cortical and trabecular densities in human and swine according with spinal locations.

Cortical bone density differences between swine and human models could be explained by the age of the sacrificed swine (approximately 4 months), as the structure of these cortical bone may still retain cartilaginous properties (Crenshaw et al. 1981). The highlighted difference in cortical bone densities could also resulted from biped vs. quadruped development of the bone microstructure.

Trabecular bones in the human cadavers could be considered osteoporotic as per the age of the subjects. Additionally, preservation technics could also alter the measured density. However, the density values reported in the results for human model are in line with the reported values for swine model.

While sawbone vertebrae have been validated for orthopedic devices testing [ASTM], densities measured by CT scan were far from the reported value by the manufacturer. Further analysis could include mechanical behavior testing of surrogate material in comparison with biological model. Investigation of the micro-structure could also furtherly explain the highlighted differences.

4. Conclusions

CT scans measurements of vertebral densities in human and swine models presented differences for cortical bones and changes in trabecular bone densities along the spine.

Choosing a surrogate for synthetic bone material will have to consider the spinal location as well as the application type (adult or pediatric).

Acknowledgements

We acknowledge the contributions of Yann Glard, Thomas Clément and Virginie Bascop for performing this study.

Disclosure statement

No potential conflict of interest was reported by the authors.

References

Aamodt A, Kvistad KA, Andersen E, Lund-Larsen J, Eine J, Benum P, Husby OS. 1999. Determination of Hounsfield value for CT-based design of custom femoral stems. J Bone Joint Surg Br. 81(1):143–7.

Ahrens J, Geveci B, Law C. 2005. ParaView: An end-user tool for large-data visualization. In: Visualization handbook. [place unknown]: Elsevier; p. 717–731.

Crenshaw TD, Peo ER, Lewis AJ, Moser BD, Olson D. 1981. Influence of age, sex and calcium and phosphorus levels on the mechanical properties of various bones in swine. J Animal Sci. 52(6):1319–1329.

Lim Fat D, Kennedy J, Galvin R, O'Brien F, Mc Grath F, Mullett H. 2012. The Hounsfield value for cortical bone geometry in the proximal humerus–an in vitro study. Skeletal Radiol. 41(5):557–68.

Morgan EF, Bayraktar HH, Keaveny TM. 2003. Trabecular bone modulus-density relationships depend on anatomic site. J Biomech. 36(7):897–904.

Morgan EF, Unnikrisnan GU, Hussein AI. 2018. Bone mechanical properties in healthy and diseased states. Ann Rev Biomed Eng. 20:119–143.

Patrick S, Birur NP, Gurushanth K, Raghavan AS, Gurudath S. 2017. Comparison of gray values of cone-beam computed tomography with hounsfield units of multislice computed tomography: an in vitro study. Indian J Dent Res. 28(1):66–70.

Stefan U, Michael B, Werner S. 2010. Effects of three different preservation methods on the mechanical properties of human and bovine cortical bone. Bone. 47(6):1048–1053.

KEYWORDS Computed tomography; bone density; spine; human; swine

morgane.evin@univ-eiffel.fr

Effect of an upper-limb exoskeleton on static postural balance

Y. Tounekti and K. Ben Mansour

Sorbonne Universities, University of Technology of Compiegne, BMBI UMR CNRS 7338, Compiegne, France

1. Introduction

The work-related Musculoskeletal disorders (MSDs) have become one of the main reasons for work absence, especially in the case of heavy charge lifting tasks. In order to prevent upper limb and back injuries, several exoskeletons were developed to assist operators while handling heavy charges. However, those devices can induce some changes in the user's posture by changing the postural stability and then rising the risk of fall, in particular back-support exoskeletons (Park et al. 2021). Furthermore, regarding upper-limb exoskeletons, is still unclear whether this type of solution increases the user's stability or not while handling different charges.

Thus, the aim of this study is to assess the influence of a new passive exoskeleton (ErgoSkel) on the postural balance during the upright quiet stance in different load conditions.

2. Methods

2.1. Experimental setup

The study was performed on 17 healthy volunteers: 7 females (mass 69kg (±6.24) ; height 166cm (±8)) and 10 males (mass 80kg (±11.63) ; height 178cm (±14)). All volunteers had no self-reported injuries or disorders and provided consent. Informed consent was obtained from each subject. This study was approved by the local ethics committee and was in accordance with the ethical standards of the 1964 declaration of Helsinki.

2.1.1. Exoskeleton

The exoskeleton used in this work is a passive upper limb wearable device: 'Ergoskel' (Ben Mansour 2020). It weighs 1.8kg. It is composed of a support in the back associated with two wires linked to hand gloves. The exoskeleton has an automatic brake to stop wires once the charge is lifted. The device aims to help the operator handle the charge by transferring it to the pelvis through the two wires and then relieving upper limb muscles.

Table 1. Differences between 2 conditions NoExo/WithExo (***) $p < 0.01$; (**) $p < 0.05$; (*) $p < 0.1$; (-) $p > 0.1$.

	0kg	5kg	10kg	15kg
X(AP)	–	***	*	***
Y(ML)	–	*	–	–
Ymax (ML)	–	–	–	**
Fcm (ML)	**	**	–	–
SD(ML)	–	–	–	***
Path	–	**	**	–
SA	–	–	–	**
LFS	–	–	–	**
SaEn (ML)	–	–	–	**

2.1.2. Material setup

To access the postural balance of the subject we measured the displacements of the center of pressure (CoP) in the anterior-posterior (AP) and medio-lateral (ML) directions using an embedded Force Platform (FP) AMTI (American Mechanical Technology, Inc., Watertown, MA). The sampling frequency of the device was 100Hz. The data were filtered using a fourth-order zero phase Butterworth low-pass filter with a cut-off frequency of 10 Hz (Ruhe et al. 2010).

2.1.3. Experimental protocol

The participants were asked to stand up opened-eyes and remain stable on the FP while handling different box masses: 0kg, 5kg, 10kg, and 15kg. All tasks were repeated in two conditions: with the exoskeleton (WithExo) and without the exoskeleton (NoExo). The tasks were randomly performed in different days. Participants were given 10 minutes to be familiarized with the device. Acquisition time was set at 45 seconds and the first 5 seconds were discarded being considered as adaptation time. Foot positions on the FP were controlled to be the same for the two conditions.

2.2. Data processing

Based on CoP displacement, 15 global and 4 structural variables were chosen from the most used in previous studies to be computed (Paillard and Noé 2015; Donker et al. 2007). Global variables indicate the resultant amplitude in both AP/ML directions such as mean CoP coordinates (X(AP), Y(ML)), the amplitude of displacement (Xmax (AP), Ymax (ML)), the mean velocity (V(AP), V(ML)), the standard deviation (SD), the mean power frequency, the mean centroidal frequency (Fcm); the sway area (SA), the path length (Path), the length function surface (LFS). Overall, the increase in global variables amplitudes indicates a loss of postural balance (Paillard and Noé 2015).

Structural parameters characterize the postural control process and were represented by: the sample entropy (SaEn), and the Lyapunov exponent (Lyap).

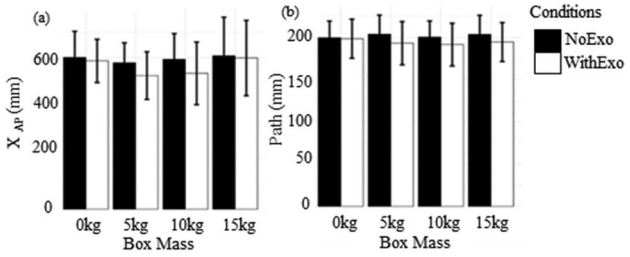

Figure 1. Bar plot (a) displacement amplitude in AP direction (b) CoP Path length.

Those variables give insight into the regularity and automaticity of the postural control process (Donker et al. 2007). Data processing was performed with MATLAB R2020b (The MathWorks, USA).

2.3. Static analysis

Shapiro-Wilk test was used to check normality distribution. As the hypothesis of normality was rejected, a non-parametric test Wilcoxon paired test (sign rank) was applied to compare CoP parameters in both conditions (NoExo/WithExo).

Furthermore, a cross-correlation analysis was carried out between all the tasks (0kg, 5kg, 10kg, and 15kg) in both conditions (NoExo/WithExo) in order to evaluate the effect of load on postural stability perturbation. Statistical analysis was performed using R software (R Core Team 2021).

3. Results and discussion

Statistical results were summarized in Table 1. Only variables presenting significant differences were represented.

For the 0kg task, there is no significant difference for almost all the CoP parameters (Table 1). This shows that wearing the exoskeleton doesn't affect the operator's postural balance. However, for 5kg and 10kg tasks there is a significant change in Path (Table 1). It decreased by 17% for both tasks in the WithExo condition (Figure 1). This could be related to the fact that the exoskeleton transfers the load on the pelvis, which reduces the amplitude of CoP AP oscillation (Figure 1).

The sway area (SA) is significantly different in the 15kg. It increased by 21% which might be due to geometry of the exoskeleton that applies an AP force on the back of the subject.

Furthermore, the sample entropy (SaEn) in the ML direction is significantly different for the 15kg task. Its decrease in the WithExo condition characterizes constraint systems with reduced adaptation and response aptitudes to potential disturbances (WithExo) and increased risk of falling (Paillard and Noé 2015). Moreover, regarding NoExo condition, results indicate that most of the global CoP variables and the lifted charge are correlated. This shows that increasing lifted loads induces a poor postural balance (Park et al. 2021).

For structural CoP parameters, we notice that there is a negative correlation. It means that structural variables decrease so that the postural control becomes more regular and less automatic which reflects poorer stability and the rise in fall risk (Donker et al.2007). Regarding WithExo condition, we noticed an improvement in CoP parameters for the 5kg and 10kg tasks. This indicates that the exoskeleton improves the postural balance for relatively small loads. However, for the 15kg task, most CoP variables show that the exoskeleton decreases the operator's stability. This could be due to the mechanical limit of the exoskeleton to transfer heavy load on the pelvis or the fact that the user needs to be trained for a better benefit (Elprama et al. 2022).

4. Conclusions

The main purpose of this study was to investigate the effect of lifting charges using an upper limb passive exoskeleton during bipedal static task conditions. The results show that the exoskeleton improves the stability parameters during 5kg and 10kg loading and is less effective for the 15kg task. Further investigations with trained users and during dynamic tasks are now performed for better insight.

Disclosure statement

No potential conflict of interest was reported by the authors.

Funding

This study is supported by the French Ministry of Higher Education, Research and Innovation and funded by FM France SAS.

References

Ben Mansour K. 2020. Non-motorized physical assistance device of exoskeleton type. Patent Int. App. No: PCT/EP2020/062098

Donker SF, Roerdink M, Greven AJ, and Beek PJ. 2007. Regularity of center-of-pressure trajectories depends on the amount of attention invested in postural control. Experim Brain Res. 181(1):1–11.

Elprama SA, Vanderborght B, and Jacobs A. 2022. An industrial exoskeleton user acceptance framework based on a literature review of empirical studies. Appl Ergonom. 100: 103615.

Paillard T and Noé F. 2015. Techniques and methods for testing the postural function in healthy and pathological subjects. BioMed Res Int. 2015:1–15.

Park J-H, Kim S, Nussbaum MA, and Srinivasan D. 2021. Effects of two passive back-support exoskeletons on postural balance during quiet stance and functional limits of stability. J Electromyogr Kinesiol. 57: 102516.

Ruhe A, Fejer R, and Walker B. 2010. The test–retest reliability of centre of pressure measures in bipedal static task conditions – a systematic review of the literature. Gait Posture. 32(4):436–45.

KEYWORDS Lifting tasks; upper limb exoskeleton; center of pressure

khalil.ben-mansour@utc.fr

Stability analysis of tensegrity mechanism coupled with a bio-inspired piping inspection robot

S. Venkateswaran[a] and D. Chablat[b]

[a]Léonard de Vinci Pôle Universitaire, Research Center, Paris La Défense, France; [b]Centre National de la Recherche Scientifique (CNRS), Laboratoire des Sciences du Numérique de Nantes (LS2N), UMR CNRS 6004, Nantes, France

1. Introduction

Piping inspection robots play an essential role for industries as they can reduce the human effort and pose lesser risker to their lives. Generally, the locomotion techniques of these robots can be classified into mechanical and bioinspired (Kassim et al. 2006). By using slot-follower leg mechanisms, DC-motors and control units, a rigid caterpillar type inspection robot was designed and developed at LS2N, France (Venkateswaran et al. 2019). This rigid prototype helped in identifying the static forces required to accomplish good contact forces with the pipeline walls. In order to work inside curvatures, a tensegrity mechanism that uses three tension springs and a passive universal joint was introduced between each module of this robot (Venkateswaran and Chablat 2019). The optimal parameters of the robot assembly were identified by considering a preloading along the cables, which ensured the stability of the entire robot (Venkateswaran et al. 2021). However, under static conditions, there exists some forces on the robot, especially on the tensegrity mechanism when one end of the leg mechanisms is clamped with the pipeline walls. These forces are dominant when the orientation of the pipeline is horizontal. The objective of this article is to understand the effect of stiffness of the spring on the static stability of the tensegrity mechanism under the self-weight of the robot assembly.

2. Methods

Similar to the static force modelling approach followed by Venkateswaran et al. (2019), the digital model of the robot is employed to analyse the tensegrity mechanism. The flexible robot in the horizontal configuration with one set of legs (left) fully clamped is shown in Figure 1. Under the condition proposed in Figure 1, the free end of the robot imposes forces and moments to the clamped end. As there are flexible tensegrity structures present between each

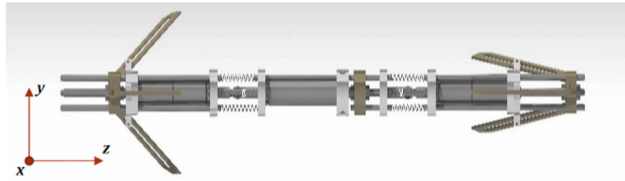

Figure 1. The piping inspection robot in the horizontal orientation.

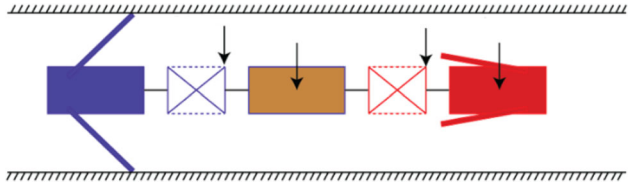

Figure 2. Distribution of masses on the robot under static condition.

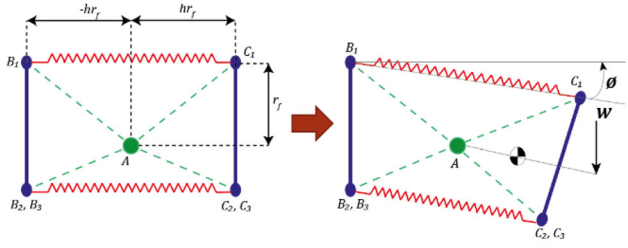

Figure 3. The tensegrity mechanism in the home-pose and loading condition.

module, the overall weight distribution for the robot could be split as shown below in Figure 2.

The tensegrity mechanism on the right end is subject to a higher amount of loading under the static condition as shown in Figure 2. The mechanism carries the weight of the entire robot, which is concentrated on the centre of gravity of the mechanism. While working inside a pipeline, the orientation of the robot about the z-axis is usually unknown. Based on earlier studies, the tensegrity mechanism undergoes the maximum deflection in the position when one of the springs is at a distance r_f from the origin. This configuration will be taken for further analysis. The geometry of the mechanism in this orientation is shown in Figure 3.

To recollect, the base coordinates of the mechansim are represented by B_1 to B_3. The moving platform coordinates are represented by C_1 to C_3. The springs are mounted at a distance r_f from the origin of each platform. The origin of the mechanism and the universal joint is at A and the tilt angles are given by α and β. When one set of leg mechanisms are clamped with the pipeline walls, the self-weight of the robot w generates a deflection of the mechanism through an angle ø. The

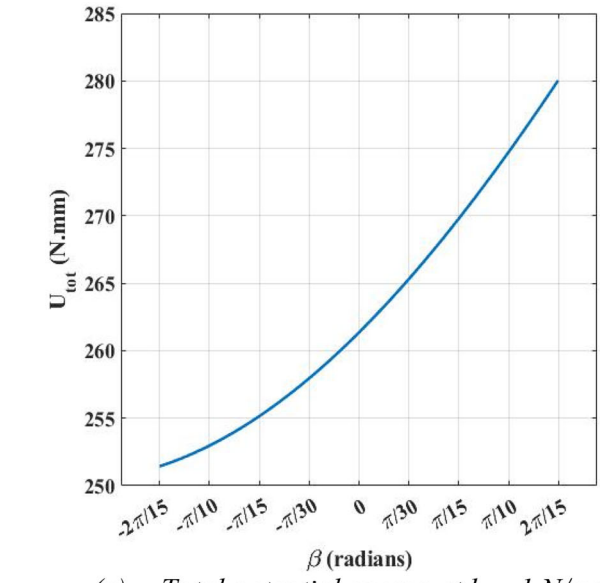

(a) Total potential energy at k = 1 N/mm

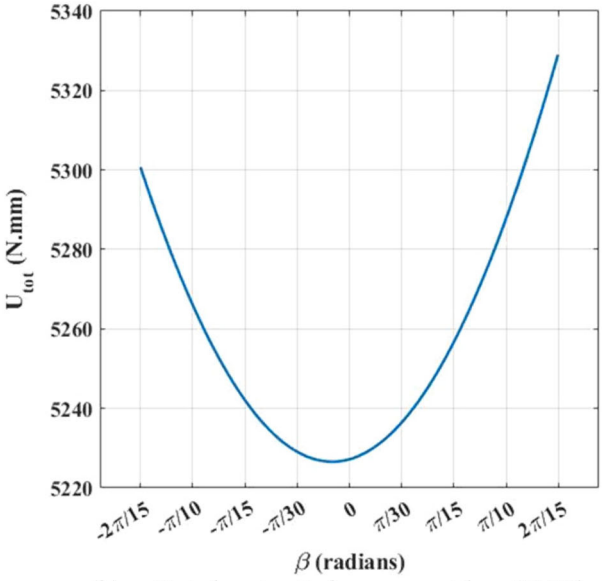

(b) Total potential energy at k = 20 N/mm

Figure 4. Total potential energy of the tensegrity mechanism under varying stiffness of spring.

self-weight is concentrated on the CG of the mechanism. The parameter h determines the static stability of the mechanism under vertical configuration and it was found to be 0.6 (Venkateswaran and Chablat 2019).

3. Results and discussion

Under static condition as demonstrated in Figure 2, the self-weight of the robot w is estimated using the digital model of the robot in CATIA. The value was found to be around 4 N. As the mechanism is studied under a passive mode, the total potential energy of the system is contributed mainly by the springs ($\boldsymbol{U_s}$) and the gravity ($\boldsymbol{U_g}$). The total potential energy ($\boldsymbol{U_{tot}}$) is given by:

$$U_{tot} = U_s + U_g \tag{1}$$

$$where\ U_s = \frac{1}{2}\ k\ \sum_{i=1}^{3} (l_i - l_o)^2$$

$$and\ U_g = \ w \sin ø\ (r_f h + CG)$$

The parameter l_o represents the zero free length of the spring and for ease of calculations, this is considered as 0 mm. From the existing prototype (Venkateswaran et al. 2021), the value of r_f was identified to be 11 mm. For the configuration represented in Figure 3b, the value of tilt angle $\alpha = 0$ radians whereas β contributes to the tilt. At this configuration, the value of ø corresponds to the value of β. By solving Eq. (1) using the design parameters specified, the total potential energy of the system is given by the equation:

$$U_{tot} = 35.2 \sin \beta + 312.8\ k - 50.82\ k \cos \beta \tag{2}$$

From Eq. (2), it can be interpreted that the stiffness of the spring k plays an essential role in the static stability of the mechanism. A value of 1 N/mm does not ensure a stable configuration. However, when the value reaches to 20 N/mm, a stable potential energy configuration could be observed. A comparison of the potential energies for the two spring stiffness values are represented in Figure 4. From Figure 4b, it can also be concluded that the total potential energy of the system can never be a minimum at 0 radians. However, with the increase in spring stiffness, the deflection of the mechanism could be significantly reduced.

4. Conclusion

The analysis presented in this article helped in understanding the static stability of the tensegrity mechanism due to the self-weigh of the robot assembly. The effect of spring stiffness on the mechanism was also understood. This study also helps in modelling the stacked tensegrity structure that will be incorporated in the robot assembly and this will permit to have an elephant trunk design.

References

Kassim I, Phee, L, Ng WS, Gong F, Dario P, Mosse CA. 2006. Locomotion techniques for robotic colonoscopy. IEEE Eng Med Biol Magaz. 25(3):49–56.

Venkateswaran, S, Chablat D, Boyer F. 2019. Numerical and experimental validation of the prototype of a bio-inspired piping inspection robot. Robotics. 8(2): 32.

Venkateswaran S and Chablat D. 2019. A new inspection robot for pipelines with bends and junctions. In IFToMM world congress on mechanism and machine science; pp. 33–42. Springer, Cham.

Venkateswaran, S, Chablat, D, Hamon, P. 2021. An optimal design of a flexible piping inspection robot. J Mech Robot. 13(3): 035002-1-14

KEYWORDS Piping inspection; bio-inspired robot; tensegrity; static analysis

swaminath.venkateswaran@devinci.fr

Numerical evaluation of a bicycle helmet during typical E-scooter falls

W. Wei[a,b], Y. Petit[b,c] and N. Bailly[a,b]

[a]LBA UMRT24, Aix Marseille Université/Université Gustave Eiffel, Marseille, France; [b]iLab-Spine – Laboratoire International en Imagerie et Biomécanique du Rachis, Marseille, France; [c]École de technologie supérieure, Montréal, Canada

1. Introduction

Electric scooters (or E-scooters) are a newly rising mode of transportation. The rapid growth of E-scooters usage has brought an increasing number of E-scooter-associated injuries (Bekhit et al. 2020) and thus rising concerns for E-scooters safety. Among all accident scenarios, E-scooters falls were reported as the most common (75.0%∼80.2%) cause of injuries for E-scooter riders (Trivedi et al. 2019; Cicchino et al. 2021). Falls initiated by the hazardous surface features (e.g. pothole) and infrastructure (e.g. curb) were the typical scenarios of E-scooter falls (Cicchino et al. 2021). Head injuries were found in 40.6%–58% of medical admissions related to E-scooter injuries and were reported as one of the most common injuries (Trivedi et al. 2019; Moftakhar et al. 2021). In a recent study, typical E-scooter falls caused by potholes were reproduced with the multi-body simulation approach to quantify the head-ground impact force and velocity (Posirisuk et al. 2022). However, this study did not investigate the risk of injury associated with these impacts nor the effect of helmet use on head acceleration and risk of injury. It is hence uncertain whether a standard bicycle helmet provides sufficient protection against head injuries during E-scooter falls. Thus the objective of this study is to evaluate the effect of using a bicycle helmet on the risk of head injury during typical E-scooter falls.

2. Methods

The finite element (FE) model of the E-scooter was developed based on the geometry of a commercially available E-scooter (Doc Green ESA 1919). The FE model of the Hybrid III 50%tile male standing dummy, developed by LSTC (Livermore Software Technology Corp., USA), was positioned on the E-scooter (Figure 1). For validation purposes, experimental E-scooter falls with a Hybrid III dummy were reproduced numerically with the FE models. In the experiment test, the falls were induced by the collision of the E-scooter with a curb at a speed of 22km/h. The head velocity during the fall and the head acceleration at head-ground impact were compared between the FE simulations and experimental tests (Figure 1).

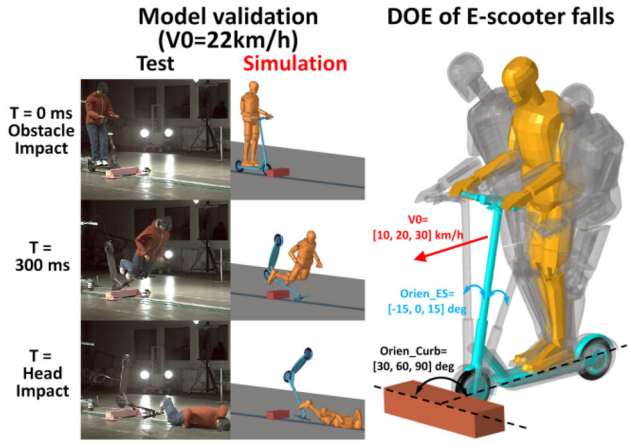

Figure 1. Comparison between experimental and numerical kinematic of the dummy during the E-Scooter fall; and model set up for typical E-scooter falls with various initial velocities (V0), E-scooter (Orien_ES) and curb (Orien_Curb) orientations.

The FE model of a helmet which passed the testing standards of bicycle helmets was worn on the E-scooter rider model. A full factorial design of experiments (DOE) was then performed with the E-scooter fall FE model to reproduce various accident scenarios with or without a helmet: different initial impact speeds (10, 20, and 30 km/h), orientations of the curb (30, 60, and 90°), and orientations of the E-scooter (−15, 0 and 15°) (Figure 1). The choice of the initial impact speeds was based on the speed limits of different countries (Trivedi et al. 2019) and the previous simulation setup (Posirisuk et al. 2022). The orientations of the curb and E-scooter were randomly chosen in this study. The head accelerations were measured during head-ground impact and the head injury criterion (HIC_36) was calculated. The helmet performance in E-scooter falls was evaluated by comparing the head acceleration and HIC_36 between FE simulations with and without a helmet. All the FE simulations were performed with the explicit solver in LS-DYNA 971 R11.1 (LSTC. Livermore, CA, USA) on an Intel Xeon (2.20 GHz) workstation with 24 processors.

3. Results and discussion

Figure 1 shows the comparison between experimental and numerical kinematic of the dummy during the E-Scooter fall: the body kinematics showed a high consistency between the simulations and experimental tests. The head displacement and velocity reproduced in the simulations were mostly within the corridors of

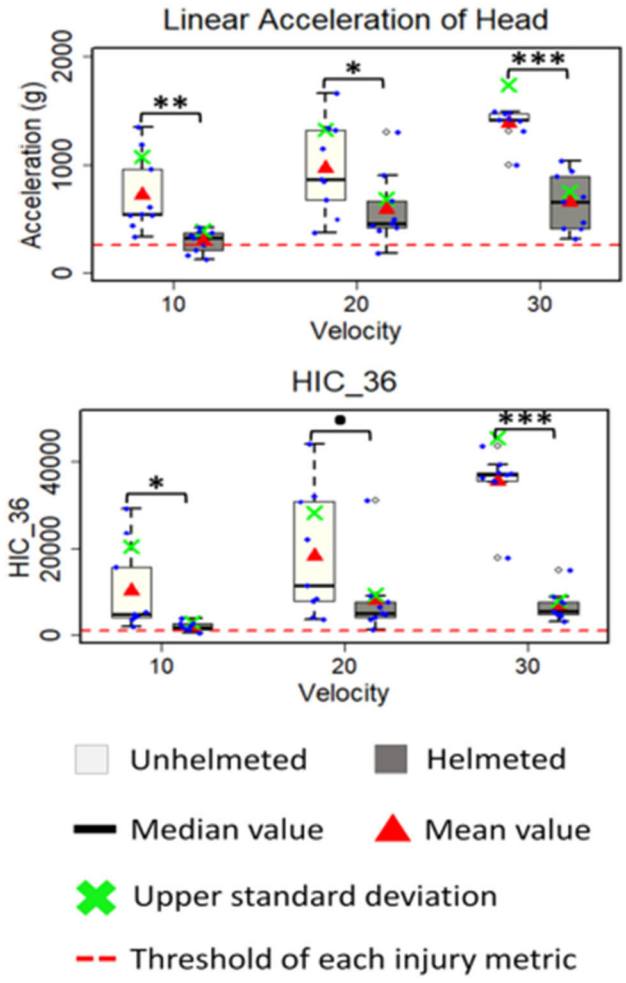

Figure 2. The effects of helmet use on head acceleration and HIC_36 during typical E-scooter falls. P values: $^{***}p < 0.001$, $^{**}p < 0.01$, $^{*}p < 0.05$, $\cdot\ p < 0.1$.

those experimental measurements. The head-ground impact time predicted in the simulation (t = 550ms) was 20ms earlier than that measured in the experiment (t = 530ms). The head linear acceleration also agreed well between the simulation (a duration of 7ms with the peak value of 681g) and the experiment (a duration of 7ms with the peak value of 622g).

Twenty-seven E-scooter falls were simulated. The forehead hit the ground first in 20 (74.1%) E-scooter falls, the face and chin hit the ground first in 5 (22.2%) cases while the rear head hit first in only one (3.7%) case. In the unhelmeted configuration, the head-to-ground impact occurred more on the forehead and with a more consistent vertical impact velocity at 30km/h than 10km/h and 20km/h. This resulted in a smaller range of head linear accelerations and HIC_36 at 30km/h than 10km/h and 20km/h. The head linear acceleration (328.5–1660.1g vs 126.2–1302.8g) and the HIC_36 (1783.3 ~ 44136.5 vs 447.0 ~ 31114.1) were found significantly ($p < 0.01$) higher in falls without a helmet than with a helmet (Figure 2).

Despite the use of a helmet, the measured HIC_36 was above the injury assessment reference value (1000) in 25 (92.6%) cases suggesting a high risk of severe head injury (AIS4+). This risk of severe head injury was predicted even when the riding speed was only 10km/h. This might be due to the high vertical velocity of head-to-ground impact (mean 5.7 m/s) induced by the rotation of the body during the fall (Figure 1).

4. Conclusions

In agreement with epidemiological data, this current study showed that typical E-scooter falls might lead to head accelerations compatible with a risk of severe head injuries. The helmet could indeed greatly reduce the head acceleration and HIC_36 during the head-ground impact in typical E-scooter falls. We thus highly recommend that E-scooter riders wear a helmet. However, despite the significant reduction in head acceleration or HIC_36 with helmet use, the predicted risk of severe injuries during helmeted falls was still high. Further work is thus needed to improve and optimize helmet designs considering the head impact conditions related to E-scooter falls: involving a higher test speed and a tangential velocity in oblique impacts.

Disclosure statement

No potential conflict of interest was reported by the authors.

References

Bekhit MNZ, Le Fevre J, Bergin CJ. 2020. Regional healthcare costs and burden of injury associated with electric scooters. Injury. 51(2):271–277.

Cicchino JB, Kulie PE, McCarthy ML. 2021. Severity of e-scooter rider injuries associated with trip characteristics. J Safe Res. 76:256–261.

Moftakhar T, Wanzel M, Vojcsik A, Kralinger F, Mousavi M, Hajdu S, Aldrian S, Starlinger J. 2021. Incidence and severity of electric scooter related injuries after introduction of an urban rental programme in Vienna: a retrospective multicentre study. Arch Orthopaed Traum Surg. 141(7):1207–1213.

Posirisuk P, Baker C, Ghajari M. 2022. Computational prediction of head-ground impact kinematics in e-scooter falls. Accid Anal Prevent. 167:106567.

Trivedi B, Kesterke MJ, Bhattacharjee R, Weber W, Mynar K, Reddy LV. 2019. Craniofacial injuries seen with the introduction of bicycle-share electric scooters in an urban setting. J Oral Maxillofac Surg. 77(11):2292–2297.

KEYWORDS e-Scooter; fall; head-ground impact; helmet; finite element

wei.wei@univ-eiffel.fr

Biomechanical analysis of the lumbosacral junction: influence of the implantation of a prosthesis on stress distribution in the vertebrae

F. Zot[a], A. Germaneau[a], M. A. Laribi[a], J. Sandoval[a], L. Caillé[a], Y. Ledoux[b], M. Mesnard[b], V. Valle[a], M. Severyns[a,d] and T. Vendeuvre[a,c]

[a]Institut Pprime, UPR 3346 CNRS – Université de Poitiers – ISAE ENSMA, Poitiers, France; [b]Institut de Mécanique et d'Ingénierie, UMR 5295 CNRS – Université de Bordeaux, Bordeaux, France; [c]Department of Orthopaedic Surgery and Traumatology, University Hospital, Poitiers, France; [d]Department of Orthopaedic Surgery and Traumatology, University Hospital, Martinique, France

1. Introduction

The management of degenerative phenomena of the spine, particularly the lumbar spine, is a major health issue. Indeed, degenerative discopathies of the lumbar spine are frequent and disabling (low back pain, radiculalgia, etc.). Surgical arthrodesis procedures (TLIF, ALIF, OLIF, etc.) have provided a relevant response to this problem (Tarpada et al. 2017). Nevertheless, the significant hindsight of these techniques has revealed mechanical complications in the medium and long term (adjacent syndromes, dislocations, etc.). This can be explained by the transfer of stress from the treated disc to the adjacent levels (Lee and Park 2016). From this observation, a new approach to the treatment of disc disease has emerged: arthroplasty. The advantage being the preservation of physiological mobility as well as a better stress distribution along the spine. However, the angular amplitudes proposed by the majority of the prostheses available on the market are larger than those allowed by the physiological disc. This may cause a stress concentration in the facet joint during movements. The objective of this work is to study the stress distribution in the facet joints after a prosthesis implantation by a coupled experiment-modelling approach.

2. Methods

2.1. Specimen

A fresh frozen human lumbar spine (L4-S1, male, 77 years old) from the laboratory of anatomy of the University of Poitiers (ABS Lab) was scanned. The volume image was analysed and segmented (3D Slicer) in order to generate the 3D numerical model.

2.2. Experimental analysis

Biomechanical tests reproducing spine physiological movements were performed by using a 7DoF Franka Emika robot to apply pure moments to our samples (Figure 1). The robot was positionally controlled for each direction: flexion/extension, lateral bending and axial rotation. Maximum amplitudes were imposed with a moment limit set at +/− 5N.m.

Two lumbar interbody prostheses were studied: Prodisc-L (Centinel Spine) and Mobidisc-L (Zimmer Biomet). The tests were performed on two types of spine segments and the results were compared: demonstrators of spinal units (3D printed, ABS) with flat endplates, and real geometry of spinal unit printed from 3D models obtained from segmentations of CT-scans of anatomic lumbar spinal segments. The lower vertebra was fixed, while the upper vertebra was linked to the robot end effector.

Moment data was provided by the robot's internal sensors, and ranges of motion were measured by an Optitrack V120 Trio camera system.

2.3. Finite element analysis

The model was created in Ansys (Ansys Mechanical Software, version 2021R2) from the segmented image of the specimen CT scan. The L4 and L5 vertebrae were extracted and a disc was created between them. Mechanical properties of annulus and nucleus are reported in Table 1. The vertebrae were modelled considering a homogenous bone material (Table 1). A cartilaginous joint was included between the articular facets of both vertebrae (Table 1). A second model was built by removing the disc and replacing it by a prosthesis offering 3 degrees of rotation. A perfect contact (totally fixed) was imposed between the vertebrae and the prosthesis endplates.

The first model was constituted by 1 090 642 tetrahedral elements, and the second one was constituted by 1 038 410 tetrahedral elements. The boundary conditions were similar as the ones imposed for the experiments.

3. Results and discussion

3.1. Experiments

Ranges of motion were measured for the demonstrator specimen and for the real geometries, and for the different studied prostheses. Table 2 presents the results obtained on the prosthesis Prodisc-L for both types of plate geometry.

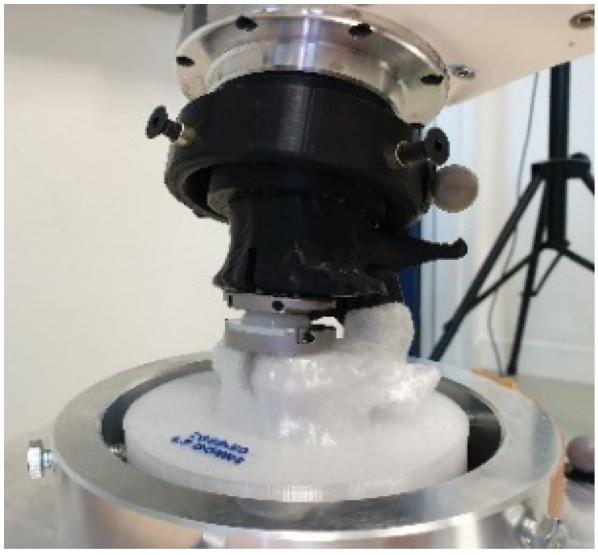

Figure 1. Loading setup with 2 vertebrae (L4 and L5) and the Prodisc-L (Centinel Spine) prosthesis.

3.2. Finite element model

Figure 2 shows an example of equivalent stress distribution in the facet joints for the model with a disc. For a moment of 5N.m in extension, we observe that the stress is particularly located on the posterior bodies of the vertebrae.

3.3. Discussion

The experiment showed that the amplitudes of each rotation were not symmetrical in the case of the real geometry. For the axial rotation test, there is significantly less movement in the case of the real geometry compared to the demonstrator. This movement reduction is caused by the presence of the facet joints. The ligamentous structures were not represented during theses tests, in order to only test the effect of the geometries on the prostheses behaviour. The specific finite element modelling provided stress distribution according to the different loadings and geometries. This study is a preliminary work to analyse stress increase produced in the posterior structures with a prosthesis offering a higher mobility than the physiological disc. An influence study must be conducted.

4. Conclusions

This study provides objective data of ranges of motions given by lumbar interbody prostheses fixed on realistic geometries and under physiological loadings. Also, data on stress distribution in the vertebrae subsequent to a prosthesis implantation was obtained.

Table 1. Mechanical properties used in the finite element model.

Structure	Young modulus (MPa)	Poisson ratio	Reference
Vertebrae	12000	0.3	(Park et al. 2013)
Annulus	8.4	0.45	(Shin et al. 2007)
Nucleus	1	0.499	(Shin et al. 2007)
Cartilage	23.8	0.4	(Ueno and Liu 1987)
Prosthesis endplates	210 000	0.3	(Rohlmann et al. 2005)

Table 2. Ranges of motion (degrees) measured for the three simulated physiological movements offered by the prosthesis Prodisc-L (Centinel Spine).

Spinal unit	Flat endplates	Real geometry
Flexion/Extension	+19.1 / −19.1	+18.5 /−12.6
Lateral Bending	+18.9 / −18.9	+14.2 / −17.5
Axial Rotation	+180 / −180	+0.24 / −0.78

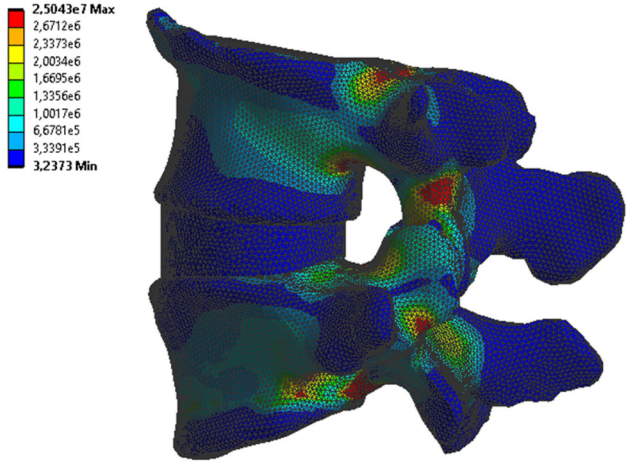

Figure 2. Stress distribution in the vertebrae for an applied moment of 5N.m in extension.

For future works, the finite element model will be completed with more spinal units, as well as different prostheses.

Disclosure statement

No potential conflict of interest was reported by the authors.

Acknowledgements

We thank the Nouvelle-Aquitaine for its financial support; companies Centinel Spine and Zimmer Biomet for having given us their prostheses; and the ABS Lab for anatomic spine segment.

References

Lee J, Park Y-S. 2016. Proximal junctional kyphosis: diagnosis, pathogenesis, and treatment. Asian Spine J. 10(3): 593.

Park WM, Kim K, Kim YH. 2013. Effects of degenerated intervertebral discs on intersegmental rotations, intradiscal pressures, and facet joint forces of the whole lumbar spine. Comput Biol Med. 43(9):1234–1240.

Rohlmann A, Zander T, Bergmann G. 2005. Effect of total disc replacement with ProDisc on intersegmental rotation of the lumbar spine. Spine. 30(7):738–743.

Shin DS, Lee K, Kim D. 2007. Biomechanical study of lumbar spine with dynamic stabilization device using finite element method. Comput Aided Des. 39(7):559–567.

Tarpada SP, Morris MT, Burton DA. 2017. Spinal fusion surgery: a historical perspective. J Orthopaed. 14(1):134–136.

Ueno K, Liu YK. 1987. A three-dimenstional nonlinear finite element model of lumbar intervertebral joint in torsion. J Biomech Eng. 109(3):200–209.

KEYWORDS Lumbar spine; lumbar prostheses; biomechanical analysis; finite element model

francois.zot@univ-poitiers.fr